







Cite this: *Nanoscale Horiz.*, 2024, 9, 742

Received 20th December 2023,  
 Accepted 26th February 2024

DOI: 10.1039/d3nh00576c

[rsc.li/nanoscale-horizons](https://rsc.li/nanoscale-horizons)

## 3D printing of layered vanadium disulfide for water-in-salt electrolyte zinc-ion batteries†

Stefano Tagliaferri,  Goli Nagaraju,  Maria Sokolikova,   
 Rachael Quintin-Baxendale and Cecilia Mattevi  \*

Miniaturized aqueous zinc ion batteries are attractive energy storage devices for wearable electronics, owing to their safety and low cost. Layered vanadium disulfide (VS<sub>2</sub>) has demonstrated competitive charge storage capability for aqueous zinc ion batteries, as a result of its multivalent states and large interlayer spacing. However, VS<sub>2</sub> electrodes are affected by quick oxide conversion, and they present predefined geometries and aspect ratios, which hinders their integration in wearables devices. Here, we demonstrate the formulation of a suitable ink for extrusion-based 3D printing (direct ink writing) based on micro flowers of layered VS<sub>2</sub> obtained using a scalable hydrothermal process. 3D printed architectures of arbitrary design present electrochemically active, porous and micron-sized struts with tuneable mass loading. These were used as cathodes for aqueous zinc-ion battery electrodes. The 3D printed VS<sub>2</sub> cathodes were assembled with carbon/zinc foil anodes to form full cells of zinc-ion, demonstrating a capacity of ~1.98 mA h cm<sup>-2</sup> with an operating voltage of 1.5 V. Upon cycling a capacity retention of around 65% was achieved after ~100 cycles. The choice of the electrolyte (a water-in-salt electrolyte) and the design of the pre-processing of the 3D printed cathode ensured improved stability against dissolution and swift oxidation, notorious challenges for VS<sub>2</sub> in an aqueous environment. This work paves the way towards programmable manufacturing of miniaturized aqueous batteries and the materials processing approach can be applied to different materials and battery systems to improve stability.

### 1. Introduction

The market of wearable devices is rapidly growing, demanding advanced energy storage systems that are safe, light and customizable.<sup>1</sup> The leading energy sources today are lithium-

#### New concepts

The electrochemical stability of VS<sub>2</sub> cathode for Zn-ion batteries *via* pre-treatment in the electrolyte has been demonstrated. The use of 3D printing (direct-ink-writing) has been demonstrated to manufacture VS<sub>2</sub> cathodes which offers sustainability, miniaturization and programmable design. So far VS<sub>2</sub> cathodes for Zn-ion batteries have been affected by quick oxidation and decomposition in the electrolyte and cathodes have been fabricated *via* drop casting or slurry coating only. This work brings new general understanding of the physico-chemical mechanism occurring at the materials/electrolyte interfaces and new approaches to ink formulation to achieve complex fluids which are 3D printable. Both these concepts can be generalized to different materials systems.

ion batteries (LIBs), and amongst those, lithium polymer batteries are utilized in wearable devices. LIBs of this type can operate at >3V and reach an energy density of 100–250 W h kg<sup>-1</sup>, making them the preferred choice for energy-demanding devices, such as mobile phones and portable electronic devices.<sup>2,3</sup> Although these batteries show several advantages, such as high energy density and lightweight design, they also come with flammability concerns and high cost.<sup>4</sup> Additionally, the customizability of such batteries, in terms of size and geometry, is limited by the manufacturing methods which are based on slot-die coating under an inert atmosphere.<sup>4–6</sup> Thus there is a growing demand for alternative solutions to power the next generation of healthcare wearable devices.<sup>7–9</sup> Wearable sensors typically present a power consumption in the range of ~0.01–1 mW, and necessitate a nominal voltage of >1.5 V to operate.<sup>10</sup> Temperature sensors based on thermistors require just ~10 μW peak power, while heart rate sensors may require a power consumption of ~100 μW.<sup>11,12</sup> In an Internet-of-things device, the power consumption of the data transmission module could also be taken into account. For example, bluetooth low energy (BLE) transmission usually requires ~50 mW.<sup>11</sup> The low power consumption of wearable sensing devices opens up the possibility of using alternative chemicals to lithium. Zinc ion batteries (ZIBs) are based on aqueous electrolytes and present a lower

Department of Materials, Imperial College London, London SW7 2AZ, UK.  
 E-mail: [c.mattevi@imperial.ac.uk](mailto:c.mattevi@imperial.ac.uk)

† Electronic supplementary information (ESI) available. See DOI: <https://doi.org/10.1039/d3nh00576c>



cradle-to-gate environmental impact than LIBs in terms of CO<sub>2</sub> emissions per kW h of energy stored.<sup>13</sup> Importantly, zinc is an earth abundant element presenting a high theoretical capacity ( $\sim 820 \text{ mA h g}^{-1}$ ), with a possibly high energy density and a conveniently low redox potential ( $-0.76 \text{ V vs. SHE}$ ) when used as an anode.<sup>14</sup> Thus ZIBs can be regarded as a possible alternative to LIBs for wearable electronic sensors and blue-tooth devices.<sup>9</sup> On the other hand, the divalent nature of zinc and high charge density of zinc ions can be detrimental for the intercalation kinetic and the structural stability of cathode materials.<sup>15</sup> As a consequence, there is a general demand to identify suitable cathodes for zinc-ion batteries. Several polymorphs of MnO<sub>2</sub> (e.g.  $\alpha$ -MnO<sub>2</sub>,  $\gamma$ -MnO<sub>2</sub> and  $\delta$ -MnO<sub>2</sub>) have been investigated as high-performance ZIB cathodes for primary and secondary batteries, owing to their low cost and high theoretical capacity.<sup>16</sup> However, MnO<sub>2</sub> cathodes are often affected by low-rate capability and cycling stability, associated with irreversible phase transitions, dissolution in the electrolyte and a large volume change during cycling.<sup>16,17</sup>

Vanadium disulfide (VS<sub>2</sub>) is a layered compound belonging to the family of transition metal dichalcogenides which has been proposed as a high-performing cathode for ZIBs, owing to its layered structure with wide spacing between the layers ( $\sim 5.76 \text{ \AA}$ ), which can easily accommodate multivalent cations.<sup>18</sup> The high-valence vanadium centres in VS<sub>2</sub> promote redox reactions with fast kinetics. In contrast to other layered cathode materials (e.g.  $\delta$ -MnO<sub>2</sub>, with a conductivity lower than  $10^{-5} \text{ S cm}^{-1}$ ),<sup>19</sup> the thermodynamically stable phase of VS<sub>2</sub> has metallic character, thus the reported electronic conductivity of vanadium sulfide can be as high as  $\sim 3 \times 10^3 \text{ S cm}^{-1}$ , which is beneficial for electron transfer and rate performance.<sup>20</sup> In comparison to vanadium oxides, which have also been widely explored for ZIBs, sulfides present larger diffusion channels and weaker interactions with multivalent cations, achieving lower migration barriers.<sup>21</sup> These favourable properties are reflected in the high capacity ( $205.3 \text{ mA h g}^{-1}$ ) and rate capability ( $135.4 \text{ mA h g}^{-1}$  at  $10 \text{ A g}^{-1}$ ) achieved when VS<sub>2</sub> is used as the cathode for zinc-ion batteries.<sup>22</sup> Additionally, it has been recently demonstrated<sup>23</sup> that it is possible to induce the growth of a stable oxide layer on VS<sub>2</sub> cathodes by controlling the working potential of the zinc battery. The resulting VS<sub>2</sub>/VO<sub>x</sub> cathodes display higher capacity ( $301 \text{ mA h g}^{-1}$ ) and greater stability (75% capacity retention after 3000 at  $1 \text{ A g}^{-1}$ ) than VS<sub>2</sub> itself. However, VS<sub>2</sub>-based cathodes still present structural dissolution and possible oxidation in aqueous ZnSO<sub>4</sub> electrolytes, which could affect the energy storage capability and long-term cycling.<sup>24</sup> Several approaches have been proposed to mitigate the dissolution of vanadium-based electrodes in ZIBs, such as surface coatings, geometry engineering, heterostructure formation and electrolyte chemistry formulation.<sup>17,25</sup> Adjusting the electrolyte concentration is an effective approach to mitigate the dissolution and the oxidation of VS<sub>2</sub> cathodes, and thus enabling longer cyclability of ZIBs. In this context, ZnCl<sub>2</sub> water-in-salt electrolytes (WISE) have been recently developed with a much higher concentration (up to  $31 \text{ mol per kg}$  of solvent) than that of conventional ZnSO<sub>4</sub> electrolytes

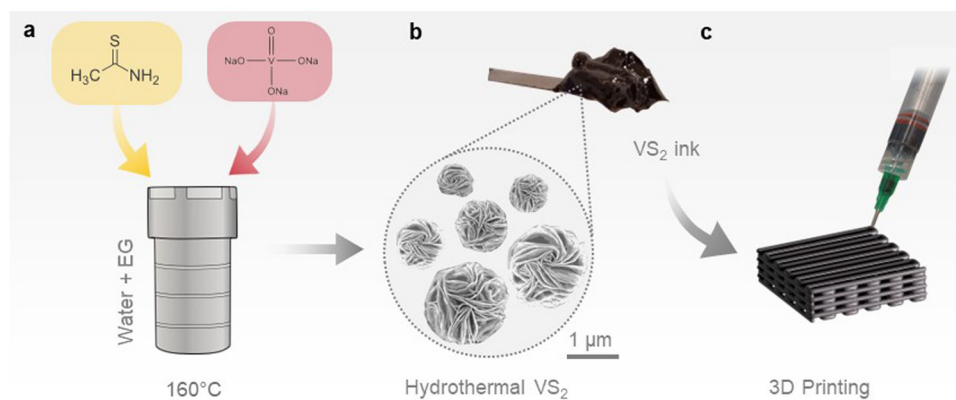
(around  $2 \text{ mol per litre}$  of solution) which improves the performance and stability of the electroactive materials in the electrodes.<sup>26,27</sup> Meanwhile, VS<sub>2</sub> cathodes for ZIBs have been mainly investigated as coin and Swagelok cells, which are not directly compatible with wearable devices. Advanced manufacturing methods, able to meet the demand for batteries with customized shape, are yet to be used for batteries. Direct ink writing is a versatile manufacturing technique that has drawn interest for the fabrication of electrodes for energy storage devices.<sup>28–32</sup> It enables the customization of the battery shape, which is a viable route to meet the requirements of wearable electronics. Additionally, it can lead to improved electrochemical performance, owing to the higher areal loading of active materials on electrodes and because the open geometry can facilitate charge transport. On the other hand, often 3D Printed electrodes rely on NMP as the dispersing solvent of the active materials to obtain printable inks for ZIBs.<sup>33–35</sup> However, NMP presents toxicity concerns, and its use aggravates the environmental impact of ZIBs, reducing the advantages over Li-ion batteries.<sup>36</sup>

In this work, we demonstrate the use of extrusion-based 3D printing (direct ink writing) as a manufacturing technique to fabricate VS<sub>2</sub> cathodes for aqueous zinc-ion batteries. The scalable hydrothermal synthesis employed for VS<sub>2</sub> ensures control over the morphology of the material, which can therefore be tailored for the 3D printing process. We formulated a novel electrically conductive ink based on layered VS<sub>2</sub> micro flowers for direct ink writing which prevents oxidation, and its printability was validated through rheological analysis. VS<sub>2</sub> inks were printed in woodpile structures over small footprint areas and utilized as the cathode in a ZIB against Zn foil anodes coated with a protective carbon layer. The notorious oxidation and dissolution of VS<sub>2</sub> in an aqueous electrolyte were mitigated by using a highly concentrated electrolyte (ZnCl<sub>2</sub> as water-in-salt electrolyte). The printed batteries can provide  $1.5 \text{ V}$  and demonstrate a capacity of  $\sim 1.98 \text{ mA h cm}^{-2}$  ( $\sim 72 \text{ mA h g}^{-1}$ ) in  $30 \text{ M ZnCl}_2$ , which can be attributed to a combination of diffusion-limited and pseudocapacitive charge storage processes. The battery shows a coulombic efficiency of  $\sim 85\%$  up to 100 cycles. These results demonstrate the viability of 3D printing to produce miniaturized and customizable energy storage devices, demonstrating the formulation of functional inks which can be produced at scale and printed in air.

## 2. Results and discussion

VS<sub>2</sub> microflowers were synthesized *via* a hydrothermal method, using a small fraction of ethylene glycol as a co-solvent. A dimethyl sulfoxide (DMSO)-based ink was subsequently formulated from the hydrothermal VS<sub>2</sub>, and employed to fabricate 3D printed cathodes, as illustrated in Scheme 1. The presence of ethylene glycol in the reaction system, with lower dielectric constant and higher viscosity than water, limits the crystal growth and leads to the formation of small VS<sub>2</sub> microflowers,  $\sim 5 \text{ \mu m}$  in diameter, as presented in the SEM images of Fig. 1a and b.<sup>37</sup>





**Scheme 1** Schematic showing the synthesis of the hydrothermal  $\text{VS}_2$  microflowers (a), the formulation of  $\text{VS}_2$  inks (b) and the 3D printing of  $\text{VS}_2$  inks to fabricate battery and supercapacitor electrodes (c).

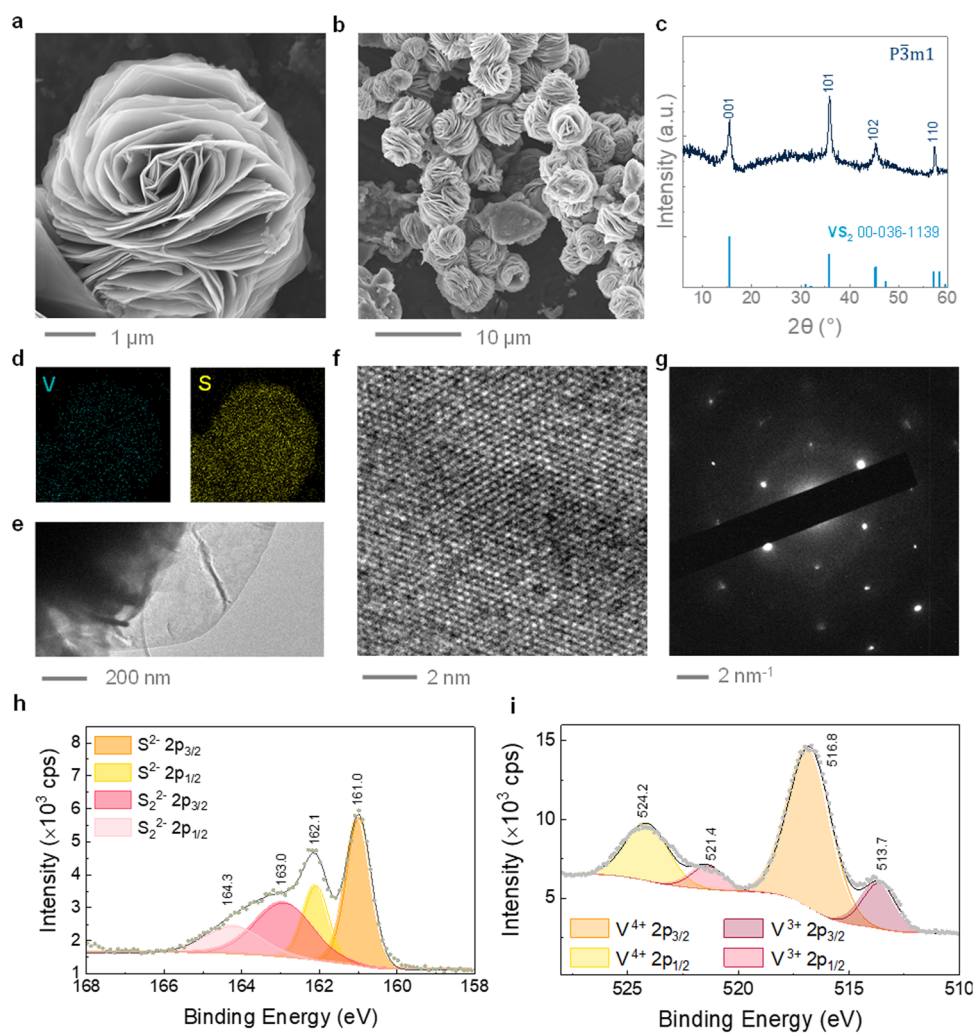


**Fig. 1** (a) and (b) High- and low-magnification SEM images of  $\text{VS}_2$  microflowers; (c) powder XRD pattern of the hydrothermal  $\text{VS}_2$  microflowers; (d) EDS spatial mapping of V ( $\text{K}\alpha$ ) and S ( $\text{K}\alpha$ ) distribution across the  $\text{VS}_2$  microflowers; (e) TEM and (f) HRTEM of a  $\text{VS}_2$  petal; (g) SAED pattern of hydrothermal  $\text{VS}_2$  along the (101) plane, (h) and (i) XPS analysis of the  $\text{VS}_2$  microflowers, high-resolution spectra corresponding to S 2p (h) and V 2p (i).



Additionally, ethylene glycol can act as a reducing agent, helping to prevent the re-oxidation of  $V^{+4}$  to  $V^{+5}$  during the synthesis. In contrast, large  $VS_2$  crystals and by-products are formed if ethylene glycol is not added (Fig. S2, ESI†). The microflower morphology is well suited for the extrusion-based 3D printing process, since microflowers can be easily ejected through small nozzles ( $< 500\ \mu\text{m}$ ) without causing obstructions resulting in flow instabilities; additionally, their porosity owing to the layered structure allows penetration of the electrolyte. The phase purity of hydrothermal  $VS_2$  was demonstrated by EDS, XRD and Raman spectroscopy (Fig. 1c and d and Fig. S1a, ESI†). All the XRD reflections can be assigned to the 1T phase of  $VS_2$  (trigonal space group  $P\bar{3}m1$ ). Similarly, the Raman modes are comparable with previous reports of hydrothermally grown  $VS_2$  with the modes at  $\sim 270\ \text{cm}^{-1}$  attributed to the in-plane vibrations and the  $\sim 410\ \text{cm}^{-1}$  to the out-of-plane vibrations.<sup>18,38</sup> Bright field TEM imaging displays the atomically thin nature of the microflower petals (Fig. 1e), while

HRTEM and SAED patterns (Fig. 1f and g) confirm that individual petals are made of highly crystalline areas. The SAED pattern shows a plane distance compatible with the (101) plane of 1T  $VS_2$ . This is consistent with previous studies on hydrothermal  $VS_2$  displaying an unusually intense (101) reflection at  $35.8^\circ$  in the XRD pattern (Fig. 1c). The two doublets in the high-resolution XPS spectrum of V 2p (Fig. 1i) indicate the coexistence of two different oxidation states for vanadium on the surface of the microflowers. The predominant doublet (largest area underneath the curve) is at binding energies of 516.8 eV and 524.2 eV which can be attributed to the  $2p_{3/2}$  and  $2p_{1/2}$  core level electrons of  $V^{4+}$ , suggesting the predominant presence of  $VS_2$ .<sup>39,40</sup> The doublet at 513.7 eV and 521.4 eV attributed to the  $2p_{3/2}$  and  $2p_{1/2}$  core level electrons corresponds to a lower oxidation state of vanadium which is likely to be  $V^{3+}$ , originating from either the reduction of the  $V^{5+}$  precursor during the synthesis or the possible presence of intercalated V atoms.<sup>41</sup> The S 2p spectrum (Fig. 1g) also presents two doublets,

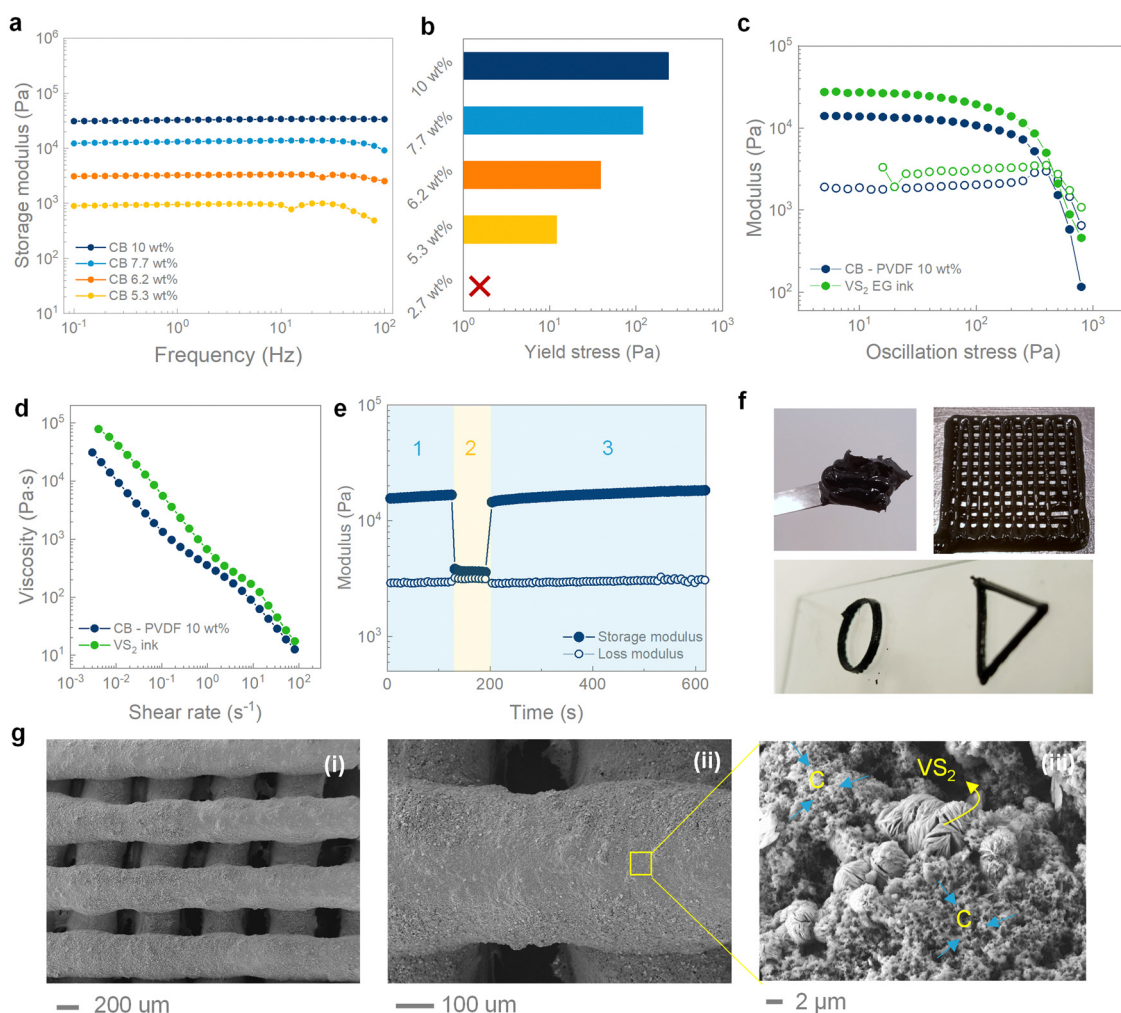


**Fig. 2** (a) Oscillatory rheology (frequency sweep) of carbon black dispersions in DMSO at different concentrations; (b) stress yield for different carbon black dispersions in DMSO; (c) amplitude sweep for the carbon black-PVDF slurry and for the final  $VS_2$  ink; (d) flow ramp for the carbon black-PVDF slurry and for the final  $VS_2$  ink; (e) three interval thixotropy tests on the  $VS_2$  ink (step 1 and 3 at a shear stress of 10 Pa, step 2 at a shear stress of 450 Pa). (f) Digital photographs showing the prepared carbon and  $VS_2$  ink (top left panel) and 3-layer woodpile structure in the top right panel; hollow ring and triangle shapes of printed  $VS_2$  electrodes on bottom panel. (g)(i–iii) Low- and high-magnification SEM images of the  $VS_2$  ink and of a printed  $VS_2$  electrode.



indicating a small presence of polysulfides ( $S_n^{2-}$ ), which probably originate from the excess free sulfides in the reaction system.<sup>42</sup>

The  $VS_2$  inks were formulated starting from a suspension of carbon black in DMSO. Carbon black particles are known to form loosely interacting aggregates in suspension, that turn into a space-filling network of connected particles above a critical concentration.<sup>43,44</sup> Concentrated suspensions behave as elastic solids at rest, while being able to flow under the action of a sufficiently high stress (yield stress), which disrupts the connectivity of carbon black particles. The existence of a finite yield stress is a key property for extrusion-based printing, since each ink layer must retain its initial shape and support the weight of the layers printed on top.<sup>32</sup> The critical concentration for carbon black suspensions in DMSO falls between 2.7 wt% and 5.3 wt%, as evidenced by oscillatory rheology (Fig. 2a and b). All the suspensions with concentrations higher than 5.3 wt% present constant viscoelastic moduli in the range of frequency investigated (0.1 to 100 Hz), with a storage modulus significantly higher than the loss modulus, indicating a gel-like behaviour and a predominantly elastic response. On the contrary, the 2.7 wt% suspension exhibits a crossover point for the viscoelastic moduli at  $\sim 2$  Hz, indicating a liquid (viscous) response in the limit of small frequencies (Fig. S1b, ESI†).<sup>45</sup> The values of storage modulus and yield stress progressively increase with concentration, reaching  $\sim 30$  kPa and  $\sim 235$  Pa at 10 wt%, respectively. At higher concentrations the suspension becomes inhomogeneous and unsuitable for extrusion. A small amount of polyvinylidene fluoride (PVDF) (9 wt%), was added to the carbon black suspension as a binder, to aid the retention of the mechanical integrity of the printed structures after solvent evaporation. The as-obtained carbon black–PVDF paste can act as a conductive ink ( $\sigma \sim 800$  S  $m^{-1}$ , Fig. S1c, ESI†) for the printing of different energy storage materials. Specifically, the addition of PVDF further increases the yield stress to  $\sim 400$  Pa, as a result of the thickening effect of the polymer (Fig. 2d). The final  $VS_2$  ink was formulated by dispersing the hydrothermal microflowers into the carbon black–PVDF paste, achieving a yield stress of  $\sim 450$  Pa and a storage modulus of  $\sim 27$  kPa (Fig. S1d, ESI† and Fig. 2d). The  $VS_2$  ink shows a shear thinning response during flow (Fig. 2e), which facilitates extrusion through fine printing nozzles. The shear thinning response can be attributed to the progressive disruption of the secondary interaction between carbon black and  $VS_2$  particles under shear, resulting in suspended aggregates with smaller hydrodynamic volumes.<sup>44</sup> The reversibility of this process is necessary to obtain self-standing structures that do not present buckling and lateral spreading on the substrate. In order to study the restructuring kinetics of the ink after shear, three interval thixotropy tests (3ITT) were performed on the final  $VS_2$  ink (Fig. 2f). The ink was at first subjected to an oscillatory stress of 10 Pa (step 1 in Fig. 2f), which falls within the linear viscoelastic region of the ink and has no destructuring effect. After 120 s of equilibration, a high oscillatory stress of 450 Pa, approximately equal to the yield stress, was applied to the ink for 10 s to break the network structure (step 2 in

Fig. 2f). Finally, an oscillatory stress of 10 Pa was applied again to the ink to study the microstructure rebuild (step 3 in Fig. 2f). After the high-stress step, the storage modulus instantly recovers to the equilibrium value, indicating the fast and reversible character of the destructuring process. Considering the favourable rheological properties, the  $VS_2$  ink could be used to 3D print electrodes with different geometries, including woodpile, hollow ring and triangle shapes showing excellent shape retention after printing (Fig. 2g). The printed structures were characterized using SEM under different magnifications (Fig. 2h), confirming the shape retention of the struts and showing how the  $VS_2$  microflowers were well intermixed with the carbon particles.

The electrochemical properties of hydrothermal  $VS_2$  cathodes were studied in a water-in-salt electrolyte (WISE) using zinc foil as the anode coated with a layer of carbon black. The role of the carbon coating is to inhibit the formation of dendrites, homogenizing the electric field and ion flux in the proximity of the anode, and delay the corrosion of zinc, which would cause capacity loss and decrease the cycling stability.<sup>46–48</sup> The highly concentrated electrolyte (30 M  $ZnCl_2$ ) was chosen to prevent the dissolution of  $VS_2$  observed in conventional aqueous electrolytes. In contrast to previous studies,<sup>18,38</sup> the dissolution of  $VS_2$  in 3 M  $ZnSO_4$  was detected by a change in the colour of the solution, which turned bright yellow (Fig. 3a). The strong UV-vis absorption below  $\sim 550$  nm can be attributed to the presence of  $VO_2^+$  ions in the sample, resulting from the oxidation of  $VS_2$  (Fig. 2b).<sup>49</sup> The dissolution of  $VS_2$  in the  $ZnSO_4$  electrolyte could also be attributed to the formation of vanadium-based complex species or due to an ionic effect where either sulfate ions ( $SO_4^{2-}$ ) or zinc ions ( $Zn^{2+}$ ) interact with the  $VS_2$ , leading to the dissolution of  $VS_2$ .<sup>50,51</sup> In contrast, the WISE electrolyte remained clear with no evidence of absorption peaks in the visible range, which suggests a good stability of  $VS_2$  in the WISE  $ZnCl_2$  electrolyte resulting from the low coordination of water molecule.<sup>52</sup> In particular, owing to the high concentration of chloride ( $Cl^-$ ) ions, not all the  $Zn^{2+}$  ions can form octahedrally coordinated complexes with water molecules, leading instead to the formation of a molten hydrate structure. As a consequence, the WISE electrolyte presents a behaviour closer to an ionic liquid one than to a conventional aqueous solution.<sup>26,53</sup> The WISE electrolyte can also aid the cycling stability of  $VS_2$ . The highly concentrated  $Cl^-$  ions hinder the dissolution processes that occur in a typical aqueous  $ZnSO_4$  electrolyte, limiting the interactions of water molecules with  $VS_2$ . The electrochemical stability of the  $VS_2$  electrodes was further examined using cyclic voltammetry in a conventional 3 M  $ZnSO_4$  and in a WISE electrolyte. While the cyclic voltammograms in the conventional 3 M  $ZnSO_4$  electrolyte are characterized by a progressive reduction of the redox current caused by the dissolution of the active material (Fig. S4a, ESI†), the current progressively increases in the WISE electrolyte, reaching a stable value after 5 cycles (Fig. S4b, ESI†). The WISE electrolyte also enables access to a larger potential window (1.5 V for 30 M  $ZnCl_2$  vs. 1.2 V for 3 M  $ZnSO_4$ ) with no significant water decomposition. Plating-stripping tests on symmetric Zn foil cells indicate that the WISE



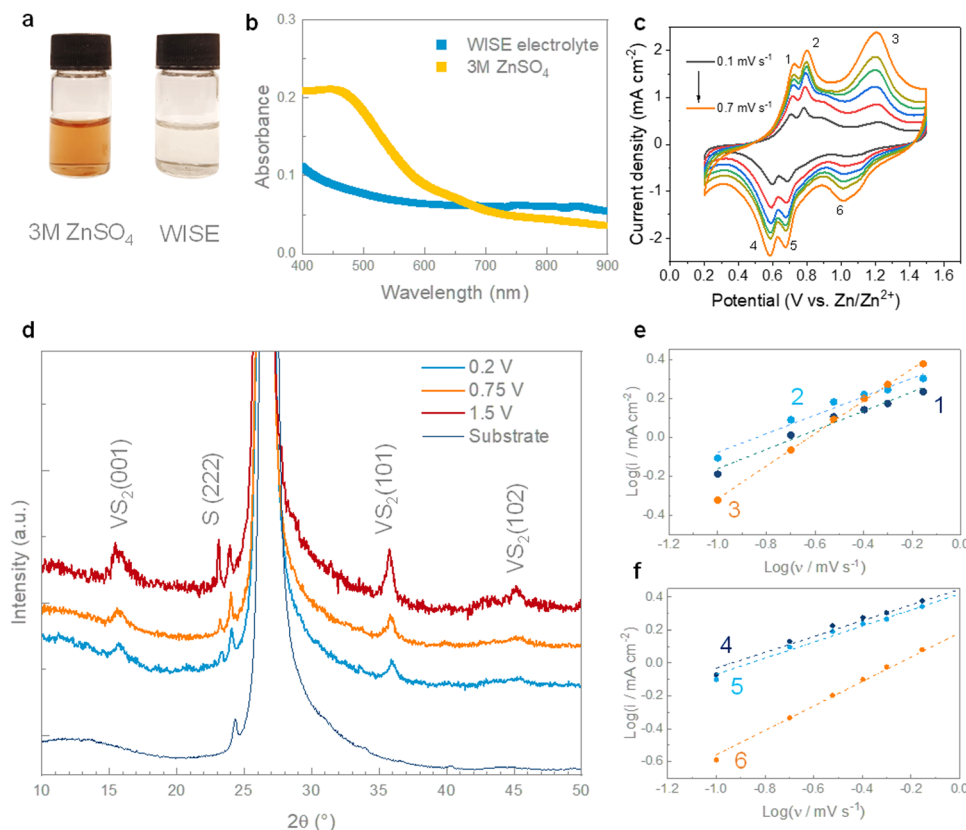


Fig. 3 (a) Digital photograph of 3 M  $\text{ZnSO}_4$  and WISE electrolytes after  $\sim 100$  h soaking of  $\text{VS}_2$ ; (b) UV-vis spectra of the 3 M  $\text{ZnSO}_4$  and WISE electrolytes after  $\sim 100$  h soaking of  $\text{VS}_2$ ; (c) cyclic voltammetry (CV) curves of ZIB using the tape-casted  $\text{VS}_2$  for kinetic analysis (measured under the scan rates of 0.1, 0.2, 0.3, 0.4, 0.5, 0.7  $\text{mV s}^{-1}$ ); (d) *ex situ* XRD on the  $\text{VS}_2$  cathodes at different state of charge; and (e) and (f) power law fitting of the redox peak currents extracted from the CV curves.

electrolyte hampers the formation of dendrites and inert byproducts, stabilizing the zinc anode for  $> 200$  h at a high current density of  $10 \text{ mA cm}^{-2}$  (Fig. S4c, ESI†). The cycling stability of symmetric cells were further extended with  $\text{C@Zn}$  electrodes, as presented in Fig. S4d (ESI†). To better understand the nature of the redox processes in the cyclic voltammetry of  $\text{VS}_2$ , we conducted kinetic analysis by fitting the redox current with a power law:<sup>54,55</sup>

$$I = a\nu^b$$

where  $i$  is the redox peak current and  $\nu$  the scan rate. When the value of  $b$  is  $\sim 0.5$  the charge storage process is diffusion limited, while when  $b \sim 1$  the charge storage has a capacitive nature. The first two oxidation peaks and the two corresponding reduction peaks (peaks 1,2,4 and 5 in Fig. 3c) have  $b$  values close to 0.5 (Table S1, ESI† and Fig. 3e and f), and they can be associated with the intercalation of  $\text{Zn}^{2+}$  ions into the layered structure of  $\text{VS}_2$ , similar to a previous report.<sup>18</sup> Differently, the redox peaks at higher potentials (peaks 3 and 6 in Fig. 3c) have broader shape and the  $b$  values are closer to 1 (0.89 and 0.79 respectively). The latter suggests the presence of capacitive processes, likely to be associated with the surface oxidation of the  $\text{VS}_2$  cathode.<sup>23</sup> The current contributions of  $\text{VS}_2$ -based ZIBs were quantified using the modified Power-law, as shown Fig. S5d and e (ESI†). As evidenced by *ex situ* XRD (Fig. 3d), there is no significant variation in the  $\text{VS}_2$  reflections

when the material is charged to different potentials, which support the evidence of the cathode stability during the first charging cycle. The shift in the (001) XRD reflection (Fig. 3d) associated with zinc intercalation and reported in previous literature<sup>18</sup> cannot be resolved using *ex situ* techniques, probably owing to the relaxation of the layered material during sample preparation.<sup>56</sup> Interestingly, a reflection at  $\sim 23^\circ$  which appears at higher charge states, could be attributed to the (222) reflection of elemental sulfur, which can plausibly originate from the formation of sulfur aggregates and the concomitant formation of sulfur vacancies in the material.<sup>41</sup> From XPS analysis during charge (Fig. S8, ESI†), the predominant oxidation state of V remains  $4+$ , although a  $\text{V}^{5+}$  component also appears possibly as a result of the surface oxidation processes. During discharge, a doublet associated with  $\text{V}^{3+}$  appears, which can be related to the creation of sulfur vacancies.

Using the 3D printed  $\text{VS}_2$  cathode,  $\text{C@Zn}$  anode, and glassy fiber membrane as a separator, we assembled a Zn-ion battery with 30 M  $\text{ZnCl}_2$  (WISE) to evaluate the energy storage performance (Fig. 4a(i)). The battery consisted of an LDPE pouch cell flooded with the WISE electrolyte. The performance of 3D printed  $\text{VS}_2$  was analysed and compared to that of tape-casted  $\text{VS}_2$  electrodes (Fig. S5a, ESI†). The 3D printed  $\text{VS}_2$  electrodes show significantly higher areal capacity ( $\sim 4.98 \text{ mA h cm}^{-2}$  vs.  $\sim 0.48 \text{ mA h cm}^{-2}$  after 10 cycles) as a consequence of the higher loading of  $\text{VS}_2$  (Fig. S5a and b, ESI†). Interestingly, the



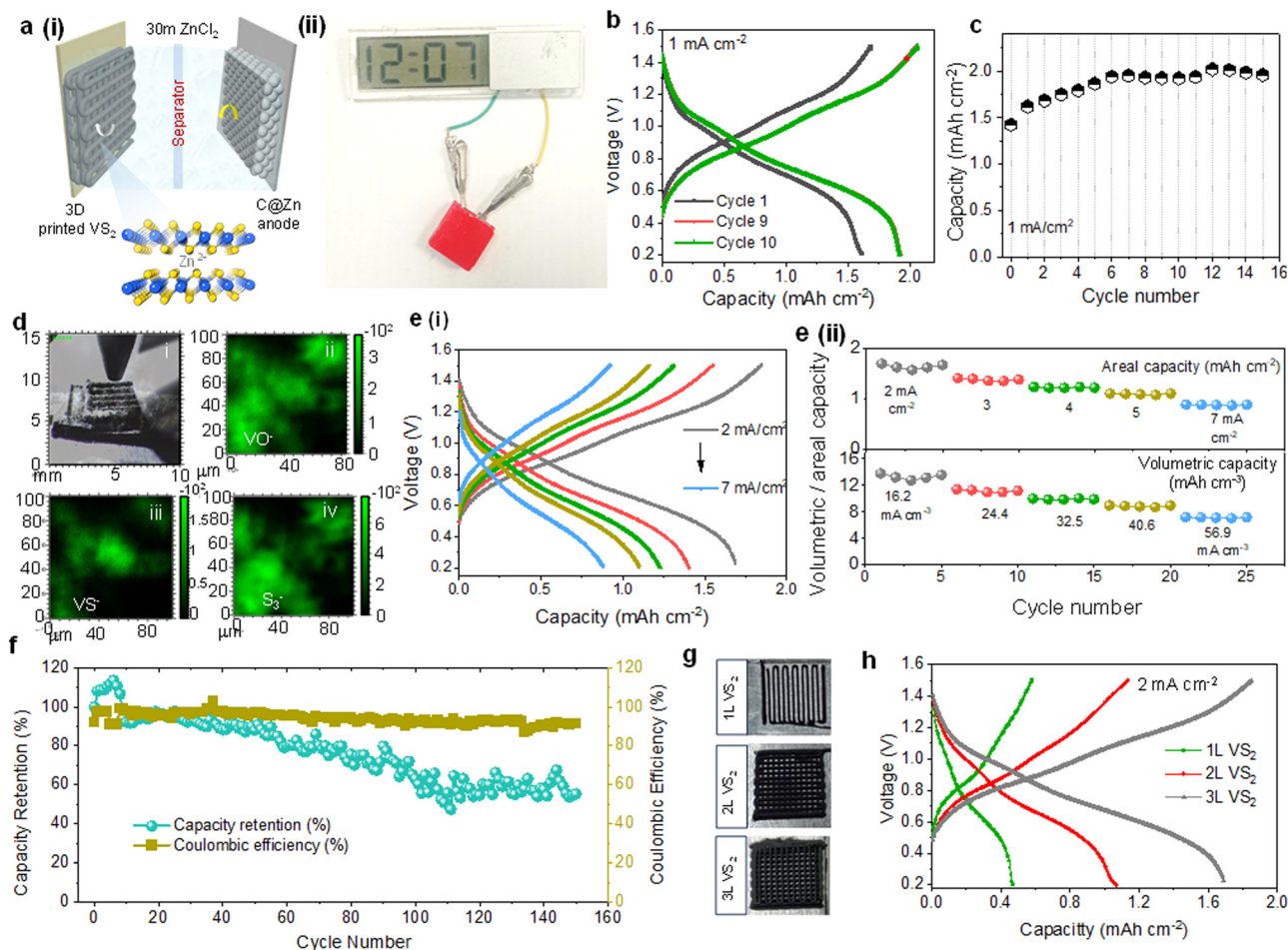


**Fig. 4** (a)(i) Schematic showing the zinc-ion battery with the 3D printed 3L  $\text{VS}_2$  cathode; (a)(ii) encapsulated zinc ion battery powering a LCD display; (b) charge–discharge curves at  $1 \text{ mA cm}^{-2}$  of the ZIB with a 3L  $\text{VS}_2$  cathode and (c) capacity during the first 15 cycles; (d) post-cycling TOF-SIMS mapping images of 3D  $\text{VS}_2$  electrode; (e)(i) charge–discharge profiles and (ii) areal capacity and volumetric capacity under different areal/volumetric current densities; (f) capacity retention over prolonged cycling of the 3D printed  $\text{VS}_2$  cathode. (g) Photographic images of 3D printed  $\text{VS}_2$  electrodes (1L, 2L and 3L  $\text{VS}_2$ ) and (h) charge–discharge plots of ZIBs using 1L–3L  $\text{VS}_2$  electrodes and C@Zn anode in 30 M  $\text{ZnCl}_2$ .

capacity of the printed cathode rapidly increases during the first  $\sim 10$  cycles, before reaching a stable performance. The increase of capacity during this activation process could be attributed to the slow penetration of electrolyte into the thick 3D electrodes and gradual transformation of  $\text{VS}_2$  into electrochemically oxidised  $\text{VS}_2$ , as reported by Yang *et al.*<sup>57</sup> When the electrodes started wetting with WISE, a rapid increment in the capacity was obtained. In order to initiate the stable electrochemical performance and prevent electrochemical conversion of the material during measurements,  $\text{VS}_2$  electrodes were preliminary soaked in the WISE electrolyte for 14 days to promote the wetting process of electrolyte into the interiors of 3D electrodes and enable the controlled growth of an electrochemically active surface layer of oxide. At a discharge current density of  $1 \text{ mA cm}^{-2}$ , the 3D printed  $\text{VS}_2$  electrodes achieved an areal capacity of  $\sim 1.6 \text{ mA h cm}^{-2}$  after soaking (vs.  $\sim 0.57 \text{ mA h cm}^{-2}$  for bare 3D printed  $\text{VS}_2$  electrodes in the first cycle, Fig. S5, ESI†), with a slightly increased response after reaching its stable value ( $\sim 1.98 \text{ mA h cm}^{-2}$ ), as presented in Fig. 4b and c. In terms of gravimetric performance, 3D printed

$\text{VS}_2$  electrodes achieved a stable gravimetric capacity of  $\sim 72 \text{ mA h g}^{-1}$  at a current density of  $36 \text{ mA g}^{-1}$  (Fig. S7, ESI†). SEM imaging demonstrates that the morphology of the microflowers is not altered during the soaking and conversion process (Fig. S6a, ESI†). After soaking in WISE, EDS and XRD spectra still show the presence of vanadium disulfide, suggesting that most likely only the surface layer of the microflowers is converted to amorphous oxide (Fig. S6b and c, ESI†). Time-of-flight secondary ion mass spectroscopy (ToF-SIMS) was used to analyse the composition of 3D  $\text{VS}_2$  electrode after repetitive charge–discharge processes ( $\sim 80$  cycles). The mapping images in Fig. 4d further confirm that the surface of 3D  $\text{VS}_2$  electrode was covered with oxygen- and sulfur- species. The rate-performance of printed ZIB was further evaluated using CD test under various current densities ( $2\text{--}7 \text{ mA cm}^{-2}$ ). The ZIB retained a capacity of  $\sim 0.88 \text{ mA h cm}^{-2}$  when discharged at a high specific current of  $7 \text{ mA cm}^{-2}$  (Fig. 4e(i) and (ii)), owing to the lower charge-transfer resistance of the printed  $\text{VS}_2$  structures ( $\sim 8.1 \Omega$ , Fig. S7(e), ESI†). We also measured the volumetric capacity of the fabricated cell, as presented in Fig. 4e(ii)



(the plot below). The device showed a maximum volumetric capacity of  $13.8 \text{ mA h cm}^{-3}$  with a capacity retention of 51.8% at a high discharge current density of  $56.9 \text{ cm}^{-3}$ . Moreover, the soaking treatment ensured a high cycling stability, with a capacity retention of  $\sim 55\%$  after 150 cycles (Fig. 4f). A 3L  $\text{VS}_2$ -based device with a  $1 \text{ cm}^2$  footprint area provided a maximum discharge power density of  $\sim 8.61 \text{ mW cm}^{-2}$  ( $70 \text{ mW cm}^{-3}$ ) and a discharge energy of  $1.28 \text{ mW h cm}^{-2}$  (Fig. S9a, ESI†). These characteristics would be sufficient to power a wide range of sensors (e.g. temperature, heart-rate and fingerprint sensors) along with their microcontroller and power management unit (with a total power consumption  $\sim 0.6 \text{ mW}$ ).<sup>11</sup> The use of the 3D printed ZIB, incapsulated in a 3D printed PLA case, to power an LED display is shown in Fig. 4a(ii) and Fig. S7c, ESI†. The effect of the number of layers forming the cathode on electrochemical performance of ZIBs was investigated. Woodpile electrodes formed by 1 layer (1L), 2L and 3L  $\text{VS}_2$  struts were manufactured (Fig. 4g and h and Fig. S7f, ESI†). The added layers have led to an increased cathode mass loading from  $12 \text{ mg cm}^{-2}$  to  $45 \text{ mg cm}^{-2}$  and consequently the areal capacity has increased from  $0.46 \text{ mA h cm}^{-2}$  to  $1.68 \text{ mA h cm}^{-2}$  (Fig. 4h and Fig. S9c–f, ESI†), as calculated from the increased redox peak current densities (Fig. S7f, ESI†). The programmable design, which allows the control of the mass loading of the electrodes and their open accessible surface, of 3D direct ink writing manufacturing is promising for driving innovations in miniaturized energy storage technology.

### 3. Conclusions

In conclusion, we have here demonstrated the use of extrusion-based 3D printing (direct ink writing) to fabricate  $\text{VS}_2$  electrodes for aqueous zinc ion batteries which are stable and cycle-life competitive with the current state-of-the-art  $\text{VS}_2$  ZIBs. The  $\text{VS}_2$  ink was optimized to achieve high storage modulus at rest ( $\sim 27 \text{ kPa}$ ), high yield stress ( $\sim 450 \text{ Pa}$ ) and fast structural recovery after shear, demonstrating good printability. The  $\text{VS}_2$  ink could thus be employed to fabricate 3D electrodes for aqueous ZIBs with a water-in-salt electrolyte (WISE). The WISE electrolyte in the zinc-ion battery effectively stabilized  $\text{VS}_2$  against dissolution and enabled improved longevity. Specifically, the 3D printed battery electrodes supplied a capacity of  $\sim 1.98 \text{ mA h cm}^{-2}$  with an operating voltage of  $1.4 \text{ V}$  and displays good reversibility up to 150 cycles with relatively stable charge and discharge curves. Benefiting from such stability, the ZIB could stably power an LCD display for several hours before discharge. These results demonstrate the feasibility of extrusion-based 3D printing as an advanced manufacturing method for stable and miniaturized free-form zinc-ion aqueous batteries based on arbitrary inorganic nanomaterials for portable and wearable electronic devices.

### 4. Methods

#### 4.1. Hydrothermal synthesis of $\text{VS}_2$

$\text{VS}_2$  was synthesized by dissolving  $11.2 \text{ mmol}$  of  $\text{Na}_3\text{VO}_4$  (Sigma-Aldrich) and  $55.9 \text{ mmol}$  of thioacetamide (Sigma-Aldrich) in

$100 \text{ mL}$  of deionized water and  $40 \text{ mL}$  of ethylene glycol. The solution was then transferred to a  $200 \text{ mL}$  PTFE-lined stainless-steel reactor and heated to  $160^\circ\text{C}$  for  $24 \text{ h}$ . The reactor was naturally cooled to room temperature and the precipitate was washed three times with ethanol and dried in a vacuum oven for  $2 \text{ h}$  at  $70^\circ\text{C}$ .

#### 4.2. Physical characterization

Scanning electron microscopy (SEM) images and EDS maps of  $\text{VS}_2$  microflowers were collected on a Zeiss Auriga SEM operated at an accelerating voltage of  $5 \text{ kV}$  (working distance  $\sim 5 \text{ mm}$ ). Powder X-ray diffraction was performed on the hydrothermal  $\text{VS}_2$  using a Bruker D2 Phaser diffractometer equipped with a copper source in the range  $2\text{--}60^\circ$  for  $2\theta$  and with an angular step size of  $0.034^\circ$ . Raman spectra were acquired using a Renishaw inVia Qontor confocal Raman microscope at a wavelength of  $532 \text{ nm}$ . X-Ray photoelectron spectroscopy (XPS) was performed using a Thermo Scientific K-Alpha+ with a monochromated Al X-ray source ( $h\nu = 1486.6 \text{ eV}$ ). The spectra were collected using pass energies of  $200 \text{ eV}$  for the survey and  $20 \text{ eV}$  for the core levels under a  $200 \mu\text{m}$  spot size. HR TEM images and ADF STEM images were acquired on a JEOL JEM-2100F microscope with a field-emission gun operated at  $200 \text{ kV}$  accelerating voltage. *Ex situ* ion mapping images of  $\text{VS}_2$  electrode were measured using time-of-flight secondary ion mass spectrometry (ToF-SIMS V system, ION-TOF GmbH) with a  $25 \text{ keV Bi}^+$  primary ion beam.

#### 4.3. Ink formulation and 3D printing

$\text{VS}_2$  inks were formulated by dispersing carbon black (acetylene, 100% compressed, Alfa Aesar) in dimethyl sulfoxide (DMSO) at  $10 \text{ wt\%}$  using a planetary mixer (Thinky ARE-250) at  $1800 \text{ rpm}$  for  $2 \text{ min}$ . Polyvinylidene fluoride (PVdF) was subsequently added to the mixture (PVdF: carbon black  $1:1$  weight ratio) and the resulting slurry was homogenized for further  $2 \text{ min}$  at  $1800 \text{ rpm}$ . Finally hydrothermal  $\text{VS}_2$  was ground in an agate mortar and the slurry was added, which was again homogenized for  $2 \text{ min}$  at  $1800 \text{ rpm}$ . The final composition of the ink was  $6:2:2$  ( $\text{VS}_2$ :PVdF:carbon black) by mass. The conductivity of the carbon black slurries was measured with 4-probe tests using a Gamry interface 1000 galvanostat. The rheological properties of the  $\text{VS}_2$  ink were measured on a rotational rheometer (discovery hybrid rheometer HR1; TA instruments) equipped with stainless-steel parallel plates ( $40 \text{ mm}$  in diameter). Oscillatory stress sweeps were performed at a fixed frequency of  $1 \text{ Hz}$ , while oscillatory recovery tests were performed at  $10 \text{ Hz}$  to maximize the acquisition of points over time. Oscillatory frequency sweeps were conducted at a fixed strain amplitude of  $0.1\%$ , within the linear viscoelastic region of the  $\text{VS}_2$  inks, as determined from the oscillatory stress sweeps. The inks were printed using an extrusion 3D printer with displacement-controlled plungers, at a feed rate of  $6 \text{ mm s}^{-1}$  and through  $410 \mu\text{m}$  nozzles. After printing (1–3 layers), the  $\text{VS}_2$  electrodes were dried overnight at room temperature followed by oven drying at  $70^\circ\text{C}/3 \text{ h}$ .

#### 4.4. Cell assembly and electrochemical testing

For electrochemical testing the  $\text{VS}_2$  ink was printed on graphite foil substrates to fabricate woodpile electrode with a thickness



between 1 and 3 layers and a footprint area of  $1\text{ cm}^2$ . Pouch-type cells were assembled using 30 M  $\text{ZnCl}_2$  electrolyte with glass fiber separators (Whatman GF/A with a thickness of  $260\text{ }\mu\text{m}$ , Sigma-Aldrich). For zinc-ion batteries, zinc foils coated with a carbon black layer were used as the anode (Fig. S3, ESI†). The carbon black layer was prepared by printing 10% PVdF-90% carbon black ink on Zn foil and was used as the anode, while the 3D printed  $\text{VS}_2$  electrode was used as the cathode during device fabrication. The electrodes were contacted with metal clips and the plastic pouch cell was sealed using parafilm.<sup>31</sup> The final volume of the packaged cell is  $\sim 0.12\text{ cm}^3$  (Fig. S7d, ESI†). For kinetic analysis, a tape-casted electrode was used instead of a 3D printed  $\text{VS}_2$  (slurry composition 7:2:1  $\text{VS}_2$ : carbon black:PVdF). Cyclic voltammetry (CV) and galvanostatic charge-discharge (GCD) and EIS curves were acquired using a multichannel VMP-3 workstation (bio-logic science instruments). A 3D printed PLA case for the ZIB was fabricated via fused deposition modelling (FDM), using a commercial Ultimaker 2+ printer. The 3D printed  $\text{VS}_2$  cathodes and zinc foil anodes (coated with a PVdF-carbon black protective layer) were inserted into the lower part of the PLA casing, which was subsequently filled with the electrolyte. The upper lid of the casing was inserted and sealed using silicone sealant. The PLA cell was connected to an LED display with stainless steel clips.

## Conflicts of interest

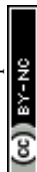
There are no conflicts to declare.

## Acknowledgements

C. M. would like to acknowledge the award of funding from the European Research Council (ERC) under the European Union's Horizon 2020 research and innovation programme (Grant Agreement No. 819069), the award of a Royal Society University Research Fellowship (UF160539), by the UK Royal Society UK and the award of EP/X037924/1 by the EPSRC. G. N. would like to acknowledge Dr Sarah Fern (Imperial College London) for SIMS analysis of cycled  $\text{VS}_2$ .

## References

- Y. Liang, C.-Z. Zhao, H. Yuan, Y. Chen, W. Zhang, J.-Q. Huang, D. Yu, Y. Liu, M.-M. Titirici, Y.-L. Chueh, H. Yu and Q. Zhang, *InfoMat*, 2019, **1**, 6–32.
- M. Li, J. Lu, Z. Chen and K. Amine, *Adv. Mater.*, 2018, **30**, 1800561.
- G. Pistoia, *Lithium-Ion Batteries: Advances and Applications*, Elsevier Science, 2013, pp. 1–694.
- T. Reddy, *Linden's Handbook of Batteries*, McGraw-Hill Education, 4th edn, 2010, p. 1456.
- M. K. Gulbinska, in *Lithium-ion Battery Materials and Engineering*, ed. M. K. Gulbinska, Springer London, London, 2014, pp. 1–29.
- B. Scrosati and J. Garche, *J. Power Sources*, 2010, **195**, 2419.
- H. Wu, D. Zhuo, D. Kong and Y. Cui, *Nat. Commun.*, 2014, **5**, 5193.
- X. Fan, B. Liu, J. Ding, Y. Deng, X. Han, W. Hu and C. Zhong, *Batteries Supercaps*, 2020, **3**, 1262–1274.
- D. Chao, W. Zhou, F. Xie, C. Ye, H. Li, M. Jaroniec and S.-Z. Qiao, *Sci. Adv.*, 2023, **6**, eaba4098.
- P. Gljušćić, S. Zelenika, D. Blažević and E. Kamenar, *Sensors*, 2019, **19**, 4922.
- M. Gao, P. Wang, L. Jiang, B. Wang, Y. Yao, S. Liu, D. Chu, W. Cheng and Y. Lu, *Energy Environ. Sci.*, 2021, **14**, 2114–2157.
- Institute of Electrical and Electronics Engineers., 2018 IEEE International Solid-State Circuits Conference, San Francisco, CA, USA, 11–15 February 2018; 474–476.
- M. Iturrondobeitia, O. Akizu-Gardoki, O. Amondarain, R. Mínguez and E. Lizundia, *Adv. Sustainable Syst.*, 2022, **6**, 2100308.
- C. Li, X. Xie, S. Liang and J. Zhou, *Energy Environ. Mater.*, 2020, **3**, 146–159.
- M. Song, H. Tan, D. Chao and H. J. Fan, *Adv. Funct. Mater.*, 2018, **28**, 1802564.
- Y. Xu, G. Zhang, J. Liu, J. Zhang, X. Wang, X. Pu, J. Wang, C. Yan, Y. Cao, H. Yang, W. Li and X. Li, *Energy Environ. Mater.*, 2023, **6**, e12575.
- F. Wan and Z. Niu, *Angew. Chem., Int. Ed.*, 2019, **58**, 16358–16367.
- P. He, M. Yan, G. Zhang, R. Sun, L. Chen, Q. An and L. Mai, *Adv. Energy Mater.*, 2017, **7**, 1601920.
- L. Yan, L. Niu, C. Shen, Z. Zhang, J. Lin, F. Shen, Y. Gong, C. Li, X. Liu and S. Xu, *Electrochim. Acta*, 2019, **306**, 529–540.
- Q. Ji, C. Li, J. Wang, J. Niu, Y. Gong, Z. Zhang, Q. Fang, Y. Zhang, J. Shi, L. Liao, X. Wu, L. Gu, Z. Liu and Y. Zhang, *Nano Lett.*, 2017, **17**(8), 4908–4916.
- M. Mao, X. Ji, S. Hou, T. Gao, F. Wang, L. Chen, X. Fan, J. Chen, J. Ma and C. Wang, *Chem. Mater.*, 2019, **31**, 3183–3191.
- H. Sun, L. Yang, E. Hu, M. Feng, C. Fan, W. Wang, H. Li, X. Wang and Z. Liu, *ACS Appl. Mater. Interfaces*, 2022, **14**, 40247–40256.
- D. Yu, Z. Wei, X. Zhang, Y. Zeng, C. Wang, G. Chen, Z. X. Shen and F. Du, *Adv. Funct. Mater.*, 2021, **31**, 2008743.
- Y. Tan, S. Li, X. Zhao, Y. Wang, Q. Shen, X. Qu, Y. Liu and L. Jiao, *Adv. Energy Mater.*, 2022, **12**, 2104001.
- H. Liu, L. Jiang, B. Cao, H. Du, H. Lu, Y. Ma, H. Wang, H. Guo, Q. Huang, B. Xu and S. Guo, *ACS Nano*, 2022, **16**(9), 14539–14548.
- C. Zhang, J. Holoubek, X. Wu, A. Daniyar, L. Zhu, C. Chen, D. P. Leonard, I. A. Rodríguez-Pérez, J. X. Jiang, C. Fang and X. Ji, *Chem. Commun.*, 2018, **54**, 14097–14099.
- T. Liang, R. Hou, Q. Dou, H. Zhang and X. Yan, *Adv. Funct. Mater.*, 2021, **31**, 2006749.
- T. S. Wei, B. Y. Ahn, J. Grotto and J. A. Lewis, *Adv. Mater.*, 2018, **30**, 1–7.
- A. Panagiotopoulos, G. Nagaraju, S. Tagliaferri, C. Grotta, P. C. Sherrell, M. Sokolikova, G. Cheng, F. Iacoviello, K. Sharda and C. Mattevi, *J. Mater. Chem. A*, 2023, **11**, 16190–16200.



- 30 S. Tagliaferri, G. Nagaraju, A. Panagiotopoulos, M. Och, G. Cheng, F. Iacoviello and C. Mattevi, *ACS Nano*, 2021, **15**, 15342–15353.
- 31 G. Nagaraju, S. Tagliaferri, A. Panagiotopoulos, M. Och, R. Quintin-Baxendale and C. Mattevi, *J. Mater. Chem. A*, 2022, **10**, 15665–15676.
- 32 S. Tagliaferri, A. Panagiotopoulos and C. Mattevi, *Mater. Adv.*, 2021, **2**, 540–563.
- 33 H. Ma, X. Tian, J. Fan, W. Cao, X. Yuan, S. Hou and H. Jin, *J. Power Sources*, 2022, **550**, 232152.
- 34 H. Ma, X. Tian, T. Wang, K. Tang, Z. Liu, S. Hou, H. Jin and G. Cao, *Small*, 2021, **17**, 2100746.
- 35 Y. Ren, F. Meng, S. Zhang, B. Ping, H. Li, B. Yin and T. Ma, *Carbon Energy*, 2022, **4**, 446–457.
- 36 Y. S. Zhang, N. E. Courtier, Z. Zhang, K. Liu, J. J. Bailey, A. M. Boyce, G. Richardson, P. R. Shearing, E. Kendrick and D. J. L. Brett, *Adv. Energy Mater.*, 2022, **12**, 2102233.
- 37 S. A. Patil, N. K. Shrestha, H. T. Bui, V. D. Chavan, D. Kee Kim, S. F. Shaikh, M. Ubaidullah, H. Kim and H. Im, *Int. J. Energy Res.*, 2022, **46**, 22070–22077.
- 38 J. Liu, W. Peng, Y. Li, F. Zhang and X. Fan, *J. Mater. Chem. C*, 2021, **9**, 6308–6315.
- 39 M. Hossain, J. Wu, W. Wen, H. Liu, X. Wang and L. Xie, *Adv. Mater. Interfaces*, 2018, **5**, 1800528.
- 40 L. Wang, K. W. Huang, J. Chen and J. Zheng, *Sci. Adv.*, 2019, **5**, eaax427.
- 41 L. He, X. Zhang, D. Yang, J. Li, M. Wang, S. Liu, J. Qiu, T. Ma, J. Ba, Y. Wang and Y. Wei, *Nano Lett.*, 2023, **23**, 7411–7418.
- 42 M. Gharabaghi, M. Irannajad and A. R. Azadmehr, *Ind. Eng. Chem. Res.*, 2012, **51**(2), 954–963.
- 43 M. Youssry, L. Madec, P. Soudan, M. Cerbelaud, D. Guyomard and B. Lestriez, *Phys. Chem. Chem. Phys.*, 2013, **15**, 14476–14486.
- 44 Y. Wang and R. H. Ewoldt, *J. Rheol.*, 2022, **66**, 937–953.
- 45 V. Trappe and D. A. Weitz, *Phys. Rev. Lett.*, 2000, **85**, 440–452.
- 46 C. Xie, Y. Li, Q. Wang, D. Sun, Y. Tang and H. Wang, *Carbon Energy*, 2020, **2**, 540.
- 47 J. Zhou, M. Xie, F. Wu, Y. Mei, Y. Hao, R. Huang, G. Wei, A. Liu, L. Li and R. Chen, *Adv. Mater.*, 2021, **33**, 2101649.
- 48 M. Zhu, J. Hu, Q. Lu, H. Dong, D. D. Karnaushenko, C. Becker, D. Karnaushenko, Y. Li, H. Tang, Z. Qu, J. Ge and O. G. Schmidt, *Adv. Mater.*, 2021, **33**, 2007497.
- 49 N. H. Choi, S. Kwon and H. Kim, *J. Electrochem. Soc.*, 2013, **160**(6), A973–A979.
- 50 Y. Tang, J. Li, C. Xu, M. Liu, B. Xiao and P. Wang, *Carbon Neutralization*, 2023, **2**, 186–212.
- 51 Y. Dong, M. Jia, Y. Wang, J. Xu, Y. Liu, L. Jiao and N. Zhang, *ACS Appl. Energy Mater.*, 2020, **3**, 11183–11192.
- 52 C. Y. Chen, K. Matsumoto, K. Kubota, R. Hagiwara and Q. Xu, *Adv. Energy Mater.*, 2019, **9**, 1900196.
- 53 W. Yang, Y. Yang, H. Yang and H. Zhou, *ACS Energy Lett.*, 2022, **7**(8), 2515–2530.
- 54 F. Wan, L. Zhang, X. Dai, X. Wang, Z. Niu and J. Chen, *Nat. Commun.*, 2018, **9**(1), 1656.
- 55 T. Brezesinski, J. Wang, S. H. Tolbert and B. Dunn, *Nat. Mater.*, 2010, **9**, 146–151.
- 56 Z. Shadike, E. Zhao, Y. N. Zhou, X. Yu, Y. Yang, E. Hu, S. Bak, L. Gu and X. Q. Yang, *Adv. Energy Mater.*, 2018, **8**, 1702588.
- 57 M. Yang, Z. Wang, H. Ben, M. Zhao, J. Luo, D. Chen, Z. Lu, L. Wang and C. Liu, *J. Colloid Interface Sci.*, 2022, **607**, 68–75.

